An acid-treated reduced graphene oxide/Mn₃O₄ nanorod nanocomposite as an enhanced anode material for lithium ion batteries†

Chae-Yong Seong,[a] Seung-Keun Park,[b] Youngkuk Bae,[a] Suyeon Yoo[a] and Yuanzhe Piao [iD] *[ac]

This work describes the preparation of an acid-treated reduced graphene oxide/Mn₃O₄ nanorod (ArGO/Mn₃O₄ NR) nanocomposite using a simple mixing and heat treatment of acid-treated graphene oxide (AGO) and MnOOH nanorods (MnOOH NRs). The as-prepared ArGO/Mn₃O₄ NR sample shows a higher performance as an anode material than bare Mn₃O₄ nanorods (Mn₃O₄ NRs) and reduced graphene oxide/Mn₃O₄ nanorods (rGO/Mn₃O₄ NR) in Li-ion batteries (LIBs). The electrochemical performance reveals that the ArGO/Mn₃O₄ NR electrode retains a higher reversible capacity of 749 mA h g⁻¹ after 100 cycles at a current density of 200 mA g⁻¹. In addition, the electrode mixed with ArGO delivers a stable capacity of 412 mA h g⁻¹ at a high current density of 2000 mA g⁻¹ while bare Mn₃O₄ NR and rGO/Mn₃O₄ NR deliver 173 and 318 mA h g⁻¹, respectively. With the advantages of facile preparation and improved electrochemical properties, the ArGO/Mn₃O₄ NR electrode can be a promising candidate as a high-performance anode material for LIBs.

Introduction

Rechargeable Li-ion batteries (LIBs) for green and sustainable energy storage are considered as the most promising power source, from portable electronics to electric vehicles.[1,2] Despite the fact that LIBs have attracted great concern due to high power density (150 W h kg⁻¹) and high energy density (400 W h L⁻¹),[3–5] graphite is not able to meet the customers' ever increasing requirements with its limited specific capacity (372 mA h g⁻¹) and poor rate capability. Accordingly, great efforts have been focused on searching for advanced anode materials with high capacity, good rate capability, and long cycle life.[6–8]

In the early 1980s, cobalt, iron and copper oxides[9–11] have been used as cathodes in primary batteries. Recently, many transition metal oxides such as manganese, cobalt and iron oxides have been further studied because of their fascinating performance as anode materials in LIBs. Among these metal oxides, Mn₃O₄ delivers a high theoretical capacity (937 mA h g⁻¹),[12–14] which is almost three times as high as that of graphite materials. Furthermore, manganese has many

advantages such as low discharge potential, high abundance, low cost, low toxicity.[15–20] In the light of the properties of manganese, Mn₃O₄ possesses a great potential as a promising anode material for LIBs. However, this anode material still suffers from large volume expansion, pulverization, poor electrical conductivity (∼10⁻⁷ to 10⁻⁸ S cm⁻¹) and unstable solid electrolyte interface (SEI) formation during Li insertion/extraction.[13,15,20–22] To overcome the above disadvantages, many new researches have been attempted in order to tackle these problems, for example Mn₃O₄ with the conductive carbon surface, composites with graphene or CNTs, mesoporous Mn₃O₄ nanotubes and sponge-like Mn₃O₄ nanostructures.[12,15,16,23–28]

Carbon materials, such as amorphous carbon, carbon nanofibers and carbon nanotubes, have proved to be a useful strategy to improve the cycling stability and the overall capacity of the transition metal oxides in LIBs because of their unique buffering ability. Recently, graphene, a single-atom-thick and two-dimensional sheet of carbon, has been suggested as the potential matrix to support transition metal oxides because of its good electrical conductivity, excellent mechanical strength, and high specific surface area.[29,30] Therefore, intensive research has been carried out to investigate the effect of graphene on the electrochemical performance of metal oxides. The results have shown that the cycling stability and the overall capacity of these oxides could be considerably improved by mixing them with graphene. In this regard, previous researches such as SnO₂/graphene, Mn₃O₄/graphene have been reported to demonstrate the improved electrochemical performance.[25,31–34] Yang *et al.*[32] showed that the SnO₂/graphene nanocomposite presented

[a]Program in Nano Science and Technology, Graduate School of Convergence Science and Technology, Seoul National University, 145 Gwanggyo-ro, Yeongtong-gu, Suwon-si, Gyeonggi-do, 443-270, Republic of Korea. E-mail: parkat9@snu.ac.kr

[b]Department of Materials Science and Engineering, Korea University, Anam-Dong, Seongbuk-Gu, Seoul 136-713, Republic of Korea

[c]Advanced Institutes of Convergence Technology, 145 Gwanggyo-ro, Yeongtong-gu, Suwon-si, Gyeonggi-do, 443-270, Republic of Korea

† Electronic supplementary information (ESI) available. See DOI: 10.1039/c7ra06396b
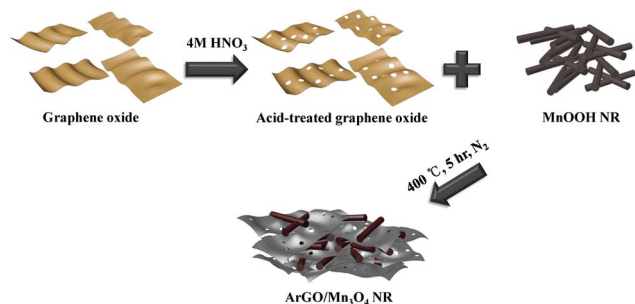
Scheme 1 Schematic preparation of nanocomposite.

a reversible capacity of 942 mA h g^{-1} at a current density of 100 mA g^{-1} after 80 cycles. Ding *et al.*[33] reported that Mn_3O_4/graphene showed a capacity of 500 mA h g^{-1} at 60 mA g^{-1} after 100 cycles. The rGO/Mn_3O_4 electrode reported in ref. 34 delivered a reversible capacity of 1294 mA h g^{-1} at 100 mA g^{-1} after 100 cycles. As a result, graphene–metal oxide nanocomposites are expected to be good candidates as anode electrodes in LIB.

In recent years, nanostructured electrode materials have been widely developed due to their improved electrochemical performance for LIBs. Among nanostructured electrode materials, one dimensional (1D) nanomaterials not only has a large surface-to-volume ratio but also provides efficient 1D electron transport pathway and short Li-ion diffusion length, which can improve the electrochemical performance in LIBs.[18,35] Furthermore, introduction of in-plane pores on graphene provides a high density of cross-plane Li^+ diffusion channels, so that reduced graphene oxides by acid treatment exhibits excellent electrochemical performance.[36,37]

The effect of the acid-treated reduced graphene oxide on the electrochemical Li-storage properties of Mn_3O_4, however, has been rarely reported. In this work, we demonstrate the preparation of $ArGO/Mn_3O_4$ nanocomposites by simple mixing and thermal treatment (Scheme 1). Mn_3O_4 NR in the nanocomposites has a high aspect ratio and is homogeneously distributed between ArGO. This structure is effective to improve electrochemical performance due to the presence of various new pores between Mn_3O_4 NR and ArGO to provide open channels and pathways for Li ions. As a consequence, ArGO/Mn_3O_4 nanocomposites exhibits a high reversible capacity and cycling stability. The $ArGO/Mn_3O_4$ nanocomposites is expected to present obviously improved electrochemical properties compared with bare oxides and reduced graphene oxide-wrapped manganese oxide nanorods.

Experimental section

Preparation of graphene oxide and acid-treated graphene oxide

The modified Hummers' method was used to synthesize graphene oxide (GO) from graphite powder (<20 micron, Aldrich).[38,39] The general synthetic procedure of GO consisted of pre-oxidation and oxidation. In the pre-oxidation step, 3 g of graphite in 80 mL of sulfuric acid (H_2SO_4, 95–98%, Aldrich) was mixed with 2.5 g of potassium persulfate ($K_2S_2O_8$, 98.0%,

SAMCHUN) and phosphorus pentoxide (P_2O_5, 97.0%, Aldrich). This solution was stirred and heated at 95 °C for 5 h. After the solution is naturally cooled down, it was vacuum-filtered and washed with DI water several times and freeze-dried overnight. In the oxidation step, 15 g of potassium permanganate ($KMnO_4$, 99.3%, Aldrich) was slowly added to 120 mL of sulfuric acid solution with the obtained powders while the acid solution was in an ice bath. After the solution was reacted at 80 °C for 4 h, hydrogen peroxide (H_2O_2, 30.0–35.5%) was added to it. The color of the solution was instantly changed from dark brown to yellow. Lastly, the mixture solution was vacuum-filtered, washed and rinsed with diluted HCl solution (1 : 10 volume ratio) and DI water to remove impurities and neutralize, followed by freeze-drying for 24 h. Acid-treated graphene oxide (AGO) was synthesized by using the process developed by Shi's group.[40] Typically, 250 mg of GO was immersed in 250 mL of nitric acid solution (4 M) and refluxed at 100 °C for 1 hour. The resulting solution was washed several times with DI water to neutralize, and then it was freeze-dried.

Synthesis of MnOOH nanorod

MnOOH nanorods were prepared by a hydrothermal method.[41] $KMnO_4$, polyethylene glycol 400 ($H(OCH_2CH_2)_nOH$, PEG-400, SAMCHUN) and DI water were prepared to obtain MnOOH NR. Typically, 0.3 g of $KMnO_4$, 7.5 mL of PEG-400 and 60 mL of DI water were stirred for 30 min until the color of the solution was changed to purple brown. The mixture in a 100 mL Teflon-lined stainless steel autoclave was heated at 160 °C for 3 h in an electric oven. Finally, the brownish product was obtained and washed several times with DI water and ethanol.

Fabrication of Mn_3O_4 NR, rGO/Mn_3O_4 NR and $ArGO/Mn_3O_4$ NR

Mn_3O_4 NR, rGO/Mn_3O_4 NR and $ArGO/Mn_3O_4$ NR were fabricated using a simple mixing and heat treatment. GO (or AGO) and MnOOH NR (3 : 1 weight ratio) were homogeneously dispersed in DI water using sonication for 30 min followed by drying at 60 °C in an electric oven. The bare and mixed powders were heated in a tube furnace at 400 °C for 5 h under N_2 atmosphere.

Material characterization

High-resolution transmission electron microscopy (HR-TEM, JEOL JEM 2100F) was performed to characterize the morphologies at an accelerating voltage of 200 kV. Field-emission scanning electron microscopy (FE-SEM, Hitachi S-4800) was used to examine the surfaces at an accelerating voltage of 0.5–30 kV. X-ray diffraction patterns of the samples were measured on an X-ray diffractometer (XRD, BRUKER D8 Advance) with Cu K$_\alpha$ radiation (α = 1.54 Å) at a scan rate of 2° min^{-1}. Brunauer–Emmett–Teller (BET) specific surface areas (SSA) and pore-size distribution were calculated by N_2 absorption/desorption isotherms on a BELSORP apparatus and Barrett–Joyner–Halenda (BJH) method, respectively.

Electrochemical measurements

CR2016-type coin cells were assembled in an Ar-filled glovebox and tested for the electrochemical performance. The electrolyte was 1 M $LiPF_6$ solution in a mixture of ethylene carbonate and dimethyl carbonate (1 : 1 volume ratio). The working electrode was fabricated by mixing 70 wt% of active material (samples), 10 wt% of binder (PVDF) and 20 wt% of conductive carbon (Super P). These materials were mixed with the n-methyl-2-pyrrolidinone (NMP) and coated onto the Cu foil by a doctor blade. After drying at 60 °C in a vacuum oven for 2 h, the coated foil was compressed and cut into circular electrodes. Electrodes were dried overnight at 120 °C in a vacuum oven and transferred to an Ar-filled glove box. All the cells were galvanostatically tested at 200 mA g^{-1} between 0.01 and 3.0 V $versus$ Li/Li$^+$ (WBCS3000 cycler system, Wonatech, Korea). Cyclic voltammetry (CV) tests were also conducted at a scan rate of 0.1 mV s^{-1} between 0.01 and 3.0 V.

Results and discussion

Fig. 1 shows the XRD patterns of MnOOH, Mn_3O_4, rGO/Mn_3O_4 and ArGO/Mn_3O_4 NR. The diffraction peaks of MnOOH NR can be indexed to a mixture of γ-MnOOH and Mn_3O_4. The results indicate that MnOOH NR is comprised of predominant γ-MnOOH and some Mn_3O_4. In the case of Mn_3O_4 NR, it consists of two phases as Mn_3O_4 and Mn_5O_8 indicating that the only MnOOH NR without GO or AGO is not completely reduced to Mn_3O_4 NR. On the other hand, the XRD peaks of rGO/Mn_3O_4 and ArGO/Mn_3O_4 nanocomposites match well to Mn_3O_4 hausmannite (JCPDS no. 24-0734). The diffraction peaks at 18.0°, 28.9°, 31.0°, 32.3°, 36.1° and 38.1° can be assigned to (101), (112), (200), (103), (211) and (004) planes of the tetragonal Mn_3O_4. As observed, the peaks of rGO and ArGO is not distinguished due to a lower content and intensity than those of Mn_3O_4 NRs. It can be reasonably deduced from the results that MnOOH NR including GO and AGO is more completely transformed to Mn_3O_4 NR.
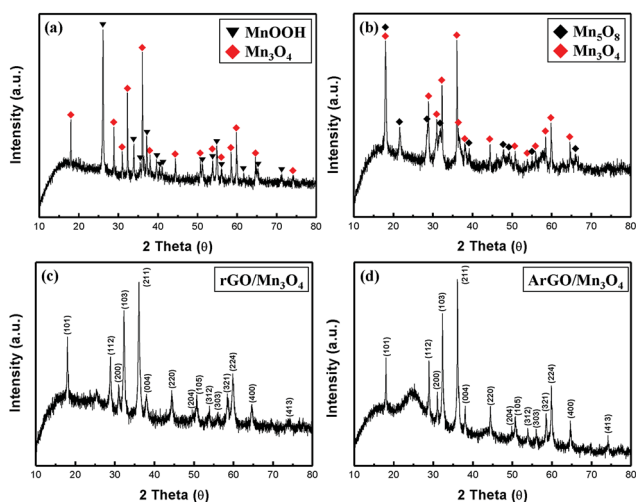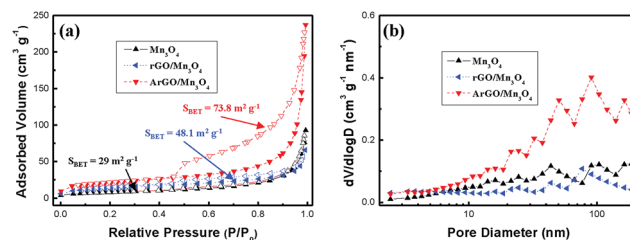

Fig. 2 (a) Nitrogen adsorption/desorption isotherms and (b) pore-size distribution of Mn_3O_4 NR, rGO/Mn_3O_4 and ArGO/Mn_3O_4.

Fig. 2 presents the nitrogen adsorption/desorption isotherms and pore-size distribution of Mn_3O_4, rGO/Mn_3O_4 and ArGO/Mn_3O_4 NR. As shown in Fig. 2a, the isotherm of the ArGO/Mn_3O_4 NR nanocomposite was classified as type IV with an H3 hysteresis loop. ArGO/Mn_3O_4 NR exhibits a higher SSA than bare Mn_3O_4 and rGO/Mn_3O_4 NR because of the restrained aggregation of the nanorods and the introduction of acid-treated graphene nanosheet with a relatively large SSA. According to BJH data, the pore-size distribution and pore volume for ArGO/Mn_3O_4 NR are much higher than those for bare Mn_3O_4 and rGO/Mn_3O_4 NR. It is believed that ArGO is contributed to SSA and pore volume.

Fig. 3 displays SEM images of MnOOH, Mn_3O_4, rGO/Mn_3O_4 and ArGO/Mn_3O_4 NR. It demonstrates that MnOOH NR was transformed to Mn_3O_4 NR without any deformation during heat treatment. After AGO (or GO) and MnOOH NR were reduced, a ArGO (or rGO)/Mn_3O_4 sandwich-like structure was finally formed due to the restacking of the hydrophobic graphene nanosheet in Fig. 3c–f. This sandwich-like structure acts as a strain buffer for volume changes of Mn_3O_4 NR during the electrochemical reaction.[42] In addition, the 1D structure of the
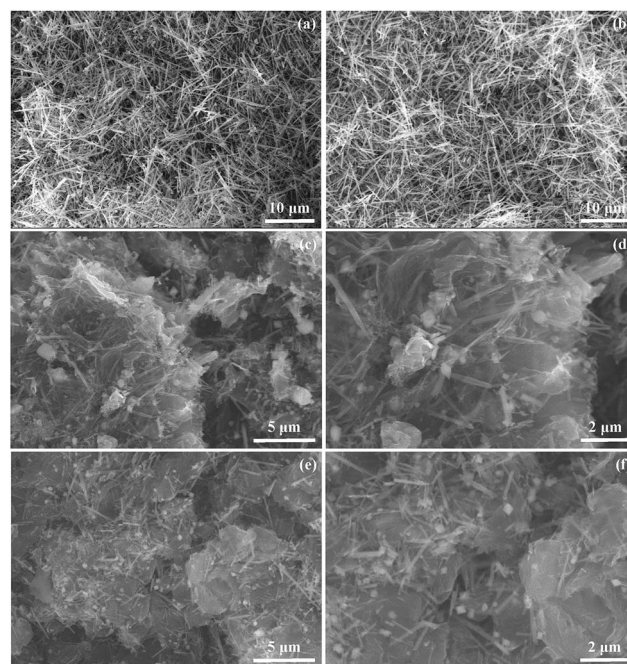

Fig. 1 XRD patterns of (a) MnOOH NR, (b) Mn_3O_4 NR, (c) rGO/Mn_3O_4 and (d) ArGO/Mn_3O_4.

Fig. 3 SEM images of (a) MnOOH, (b) Mn_3O_4, (c, d) rGO/Mn_3O_4 and (e, f) ArGO/Mn_3O_4 NR.
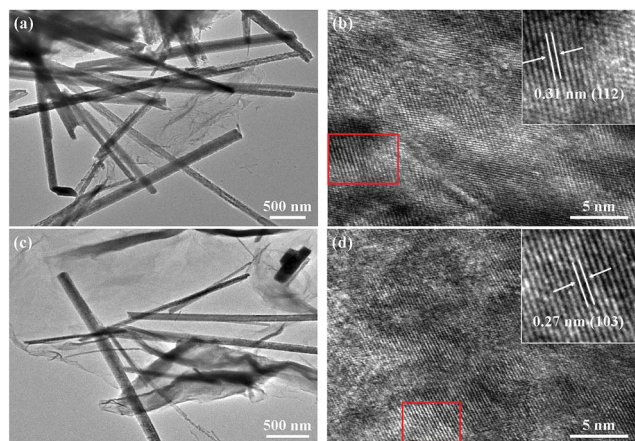
Fig. 4 TEM and HR-TEM images of (a, b) rGO/Mn_3O_4 and (c, d) ArGO/Mn_3O_4 NR.

Fig. 5 Cyclic voltammograms and charge–discharge profiles of (a, b) Mn_3O_4, (c, d) rGO/Mn_3O_4 and (e, f) ArGO/Mn_3O_4 NR.

nanorods provides a short diffusion length for Li-ion and electron transport along the 1D direction. Through the transparent rGO and ArGO, it is clear that Mn_3O_4 NR is confined in between graphene nanosheets, which provide the pathway and open channel for Li-ions and electrons, respectively. A large contact interface between electrode and electrolyte is also formed in this structure. Furthermore, Fig. 3c–f clearly indicates that Mn_3O_4 NR in the nanocomposite is uniformly distributed and continuously interconnected with rGO and ArGO. As a consequence of the ArGO (rGO)/Mn_3O_4 NR structure, it is anticipated that the electrolyte wettability over the entire nanocomposite and an effective diffusion for lithium ions and electrons is favorable. The morphology of the ArGO/Mn_3O_4 NR after 100 cycles was also characterized by SEM as shown in Fig. S1.† Mn_3O_4 nanorods still retains their 1D structure and SEI around them is observed. It confirms that ArGO nanosheets function as buffer layers to prevent the volume change of Mn_3O_4 NR.

The crystalline structure and morphology of Mn_3O_4, rGO/Mn_3O_4 and ArGO/Mn_3O_4 NR were further studied by TEM and HR-TEM, as shown in Fig. 4. Without any structural variation, Mn_3O_4 NR (Fig. 4a) was formed after heat treatment, which is well matched with SEM results (Fig. 3a and b). In HR-TEM image of rGO/Mn_3O_4 and ArGO/Mn_3O_4 NR (the inset of Fig. 4d and f), Mn_3O_4 NR clearly have crystal lattice fringes of 0.31 and 0.27 nm, corresponding to the (112) and (103) planes, respectively.

Cyclic voltammetry (CV) tests were performed at a scan rate of 0.1 mV s^{-1} between 0.01 and 3 V to understand the redox reactions to Mn_3O_4 NR, rGO/Mn_3O_4 NR and ArGO/Mn_3O_4 NR as anode materials. The 1st, 2nd, 5th and 10th of CV curves for all electrodes are presented in the Fig. 5a, c and e. In the first cycle of the Mn_3O_4 NR electrode, a broad cathodic peak in the range of 0.5–1.9 V was observed and disappeared in the following cycles, which is ascribed to the formation of solid electrolyte interfaces (SEI) due to the electrolyte decomposition[43] and the reduction of Mn_3O_4 (Mn^{3+}) to MnO (Mn^{2+}).[16] In addition, the strong cathodic peak centered at 0.035 V is attributed to the reduction of MnO (Mn^{2+}) to Mn (Mn^0). After the first cycle, the
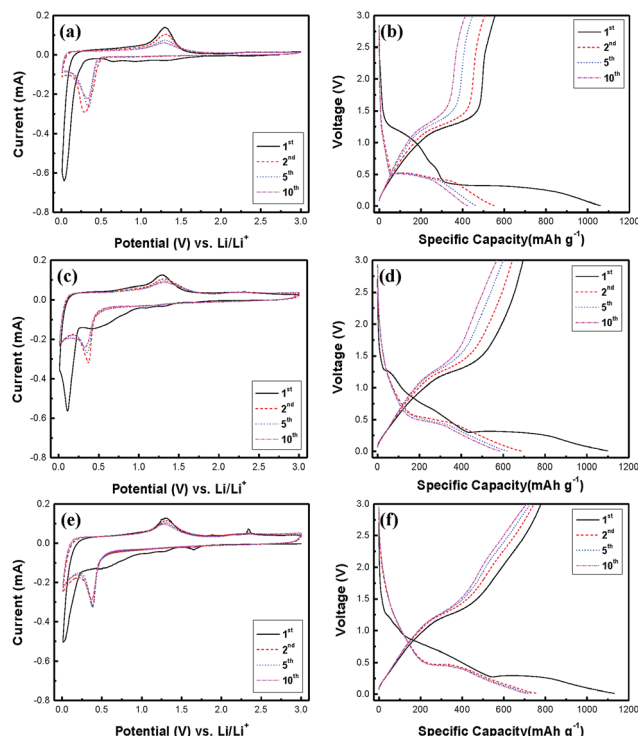
reduction peak shifts from 0.035 to *ca.* 0.35 V because of the structural transformations during the first discharge.[13,44–47] The anodic peak at 1.3 V corresponds to the oxidation of Mn to MnO.[16] For the Mn_3O_4 NR electrode, this peak intensity decreases drastically which means the poor reversibility. As shown in the Fig. 5c, the CV curve for the rGO/Mn_3O_4 demonstrates the effect of reduced graphene oxides when Mn_3O_4 NR is mixed with rGO. Unlike the Mn_3O_4 electrode, the reversible capacity of the rGO/Mn_3O_4 electrode is pronouncedly enhanced. In the case of the ArGO/Mn_3O_4 electrode, there is another anodic peak at 2.34 V which is related with the further oxidation of MnO to Mn_3O_4.[14,15,17,19,25,48,49] Furthermore, the cathodic peak at 1.65 V is clearly observed and associated with the reduction of Mn_3O_4 to MnO. It is anticipated that lithium ions may easily pass through graphene sheets without detouring. As a result of the CV curves, ArGO/Mn_3O_4 electrode displays a higher reversible capacity than Mn_3O_4 and rGO/Mn_3O_4 electrodes. Based on the CV analyses and the previous studies,[50] the mechanism for the electrochemical conversion reaction between Li and Mn_3O_4 can be expressed by the following equation:
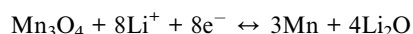
$$Mn_3O_4 + 8Li^+ + 8e^- \leftrightarrow 3Mn + 4Li_2O$$

Fig. 5b, d and f shows the 1st, 2nd, 5th and 10th charge–discharge curves for all electrodes at a current density of 200 mA g^{-1} between 0.01 and 3 V. The curves are well-matched with the previous reports on[12,15,16,24–27] the charge–discharge trend of Mn_3O_4 anodes. During the first discharge, the voltage plateau at 1.25 V is sloping down to 0.27 V, which is mainly attributed to

the SEI formation and the initial reduction of Mn_3O_4 to MnO.[15,25] The long voltage plateau from 0.27 V to 0.01 V indicates that MnO is further reduced to Mn.[13,15] After the first cycle, the plateau at 0.27 V moves up to 0.45 V, which implies that lithium ions can readily react with MnO in the following cycles. On the other hand, the voltage plateau at 1.25 V results from the oxidation of Mn to MnO while the electrodes are charging.[15]

Mn_3O_4, rGO/Mn_3O_4 and ArGO/Mn_3O_4 electrodes deliver a first discharge capacity of 1060, 1100 and 1130 mA h g^{-1} and then a reversible capacity of 556, 695 and 778 mA h g^{-1}, respectively. The ArGO/Mn_3O_4 electrode exhibits a lower initial irreversible capacity of 32% than those of 48 and 37% for Mn_3O_4 and rGO/Mn_3O_4 electrodes, respectively. The capacity loss for the first cycle is mainly due to the SEI formation by the decomposition of electrolyte and the large volume change which is the common phenomenon relating to the conversion reaction for anode materials. Coulombic efficiency (CE) increases to 98% after 3 cycles. The reversible capacity reaches to 749 mA h g^{-1} after 100 cycles, higher than other anode materials.

Among all electrodes, the ArGO/Mn_3O_4 electrode presents the most excellent reversibility because acid-treated reduced graphene oxides have the performance of the electrode improved. Consequently, the ArGO/Mn_3O_4 electrode has more stable and reversible charge–discharge process than other electrodes due to acid treatment of graphene oxide, which may promote the transportation for lithium ions and electrons through ArGO sheets.

The cycle performance tests of electrodes were performed at a current density of 200 mA g^{-1} and the results were given in Fig. 6a. The initial charge capacity is 778 mA h g^{-1}, and thereafter, the capacity decreases gradually. However, it is interesting that a gradual increase of capacity is also observed after the capacity reaches a minimum capacity. A high capacity of 749 mA h g^{-1} is achieved after 100 cycles. This capacity variation has been reported on many transitional metal oxides, particularly nanostructured Mn_xO_y.[51–53] Lowe and co-workers proposed that the extra capacity may be contributed to a capacitive-like charge storage.[54] Yonekura et al. suggested that the increasing capacity was caused by the degradation of electrolyte.[55] This phenomenon, proposed by J. M. Tarascon, might be related to the reversible growth of a polymeric gel-like film catalyzed by 3d metals.[56] The capacity increases that comes from activation of electrode materials could be another possibility. In other words, small nanoparticles not only increase the surface area but also

active sites for lithium storage. The polymeric gel-like SEI layer which can improve the mechanical cohesion among the active materials without hindering the ion transfer is formed by the electrolyte decomposition.

The rate performance of bare Mn_3O_4, rGO/Mn_3O_4 and ArGO/Mn_3O_4 nanocomposites from 100 to 2000 mA g^{-1} is shown in Fig. 6b. The ArGO/Mn_3O_4 electrode delivers a high capacity of 948, 778, 597, 509, and 412 mA h g^{-1} at different current densities of 100, 200, 500, 1000, and 2000 mA g^{-1}, respectively. When the current density returned to 100 mA g^{-1}, the discharge capacity of the ArGO/Mn_3O_4 electrode remarkably recovered to 802 mA h g^{-1}. This performance presents that a high current density doesn't affect the ArGO/Mn_3O_4 electrode.

Conclusions

In this research, a simple and two-step process such as mixing and heat treatment was applied to fabricating the ArGO/Mn_3O_4 NR nanocomposite. Mn_3O_4 NR between ArGO layers is homogeneously dispersed, thus preventing aggregation of nanorods. The nanocomposite structure of ArGO and Mn_3O_4 NR not only forms large contact areas between electrolyte and electrode but also provide the effective diffusion pathways for Li-ions and electrons. As a result, the ArGO/Mn_3O_4 NR electrode delivers reversible capacities of 778 and 412 mA h g^{-1} at 200 and 2000 mA g^{-1}, respectively, which are higher than those of bare Mn_3O_4 NR and rGO/Mn_3O_4 NR. It is expecting that ArGO/other metal oxides nanocomposites will be developed to improve the anode performance for energy storage devices.

Acknowledgements

Notes and references

1 M. S. Whittingham, Chem. Rev., 2004, 104, 4271.
2 M. Armand and J. M. Tarascon, Nature, 2008, 458, 652.
3 J. M. Tarascon and M. Armand, Nature, 2001, 414, 359.
4 P. G. Bruce, B. Scrosati and J. M. Tarascon, Angew. Chem., Int. Ed., 2008, 47, 2930.
5 S. Goriparti, E. Miele, F. De Angelis, E. Di Fabrizio, R. Proietti Zaccaria and C. Capiglia, J. Power Sources, 2014, 257, 421.
6 B. Dunn, H. Kamath and J. M. Tarascon, Science, 2011, 334, 928.
7 N. S. Choi, Z. Chen, S. A. Freunberger, X. Ji, Y. K. Sun, K. Amine, G. Yushin, L. F. Nazar, J. Cho and P. G. Bruce, Angew. Chem., Int. Ed., 2012, 51, 9994.
8 M. G. Kim and J. Cho, Adv. Funct. Mater., 2009, 19, 1497.
9 M. M. Thackeray, S. D. Baker and J. Coetzer, Mater. Res. Bull., 1982, 17, 405.

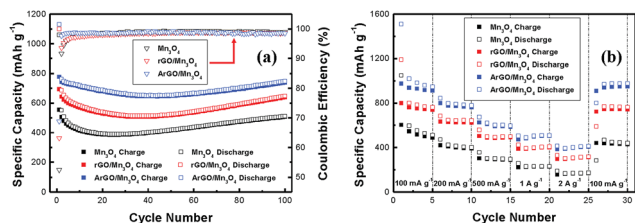Fig. 6 Comparative cycle performance of Mn_3O_4 NR, rGO/Mn_3O_4 NR and ArGO/Mn_3O_4 NR at a current density of 200 mA g^{-1} and rate capability of Mn_3O_4 NR, rGO/Mn_3O_4 NR and ArGO/Mn_3O_4 NR at various current densities.

10 M. M. Thackeray and J. Coetzer, *Mater. Res. Bull.*, 1981, **16**, 591.

11 T. Iijima, Y. Toyoguchi, J. Nishimura and H. Ogawa, *J. Power Sources*, 1980, **5**, 99.

12 H. Wang, L. F. Cui, Y. Yang, H. S. Casalongue, J. T. Robinson, Y. Liang, Y. Cui and H. Dai, *J. Am. Chem. Soc.*, 2010, **132**, 13978.

13 J. Z. Wang, N. Du, H. Wu, H. Zhang, J. X. Yu and D. Yang, *J. Power Sources*, 2013, **222**, 32.

14 C. J. Chae, J. H. Kim, J. M. Kim, Y. K. Sun and J. K. Lee, *J. Mater. Chem.*, 2012, **22**, 17870.

15 J. Gao, M. A. Lowe and H. c. D. Abruña, *Chem. Mater.*, 2011, **23**, 3223.

16 Z. C. Bai, N. Fan, Z. C. Ju, C. L. Guo, Y. T. Qian, B. Tang and S. L. Xiong, *J. Mater. Chem. A*, 2013, **1**, 10985.

17 S. Z. Huang, J. Jin, Y. Cai, Y. Li, H. Y. Tan, H. E. Wang, G. Van Tendeloo and B. L. Su, *Nanoscale*, 2014, **6**, 6819.

18 Z. C. Bai, X. Y. Zhang, Y. W. Zhang, C. L. Guo and B. Tang, *J. Mater. Chem. A*, 2014, **2**, 16755.

19 G. Q. Jian, Y. H. Xu, L. C. Lai, C. S. Wang and M. R. Zachariah, *J. Mater. Chem. A*, 2014, **2**, 4627.

20 A. Ponrouch, P. L. Taberna, P. Simon and M. R. Palacín, *Electrochim. Acta*, 2012, **61**, 13.

21 D. Pasero, N. Reeves and A. West, *J. Power Sources*, 2005, **141**, 156.

22 Q. Fan and M. S. Whittingham, *Electrochem. Solid-State Lett.*, 2007, **10**, A48.

23 C. Wang, L. Yin, D. Xiang and Y. Qi, *ACS Appl. Mater. Interfaces*, 2012, **4**, 1636.

24 S. Y. Liu, J. Xie, Y. X. Zheng, G. S. Cao, T. J. Zhu and X. B. Zhao, *Electrochim. Acta*, 2012, **66**, 271.

25 L. Li, Z. Guo, A. Du and H. Liu, *J. Mater. Chem.*, 2012, **22**, 3600.

26 N. Lavoie, P. R. L. Malenfant, F. M. Courtel, Y. Abu-Lebdeh and I. J. Davidson, *J. Power Sources*, 2012, **213**, 249.

27 Z. H. Wang, L. X. Yuan, Q. G. Shao, F. Huang and Y. H. Huang, *Mater. Lett.*, 2012, **80**, 110.

28 S. Luo, H. C. Wu, Y. Wu, K. L. Jiang, J. P. Wang and S. S. Fan, *J. Power Sources*, 2014, **249**, 463.

29 A. K. Geim and K. S. Novoselov, *Nat. Mater.*, 2007, **6**, 183.

30 K. S. Novoselov, A. K. Geim, S. V. Morozov, D. Jiang, M. I. Katsnelson, I. V. Grigorieva, S. V. Dubonos and A. A. Firsov, *Nature*, 2005, **438**, 197.

31 C. M. Chen, Q. Zhang, J. Q. Huang, W. Zhang, X. C. Zhao, C. H. Huang, F. Wei, Y. G. Yang, M. Z. Wang and D. S. Su, *J. Mater. Chem.*, 2012, **22**, 13947.

32 H. Zhang, L. Gao and S. Yang, *RSC Adv.*, 2015, **5**, 43798.

33 Y. Ren, J. Wang, X. Huang, B. Yang and J. Ding, *RSC Adv.*, 2015, **5**, 59208.

34 I. Nam, N. D. Kim, G.-P. Kim, J. Park and J. Yi, *J. Power Sources*, 2013, **244**, 56.

35 D. K. Kim, P. Muralidharan, H. W. Lee and R. Ruffo, *Nano Lett.*, 2008, **8**, 3948.

36 X. Zhao, C. M. Hayner, M. C. Kung and H. H. Kung, *ACS Nano*, 2011, **5**, 8739.

37 N. Wang, J. Yue, L. Chen, Y. Qian and J. Yang, *ACS Appl. Mater. Interfaces*, 2015, **7**, 10348.

38 W. S. Hummers and R. E. Offeman, *J. Am. Chem. Soc.*, 1958, **80**, 1339.

39 N. I. Kovtyukhova, P. J. Ollivier, B. R. Martin, T. E. Mallouk, S. A. Chizhik, E. V. Buzaneva and A. D. Gorchinskiy, *Chem. Mater.*, 1999, **11**, 771.

40 X. Wang, L. Jiao, K. Sheng, C. Li, L. Dai and G. Shi, *Sci. Rep.*, 2013, **3**, 1996.

41 Z. Bai, N. Fan, Z. Ju, C. Sun and Y. Qian, *Mater. Lett.*, 2012, **76**, 124.

42 J. Su, M. Cao, L. Ren and C. Hu, *J. Phys. Chem. C*, 2011, **115**, 14469.

43 S. Grugeon, S. Laruelle, R. Herrera Urbina, L. Dupont, P. Poizot and J. M. Tarascon, *J. Electrochem. Soc.*, 2001, **148**, A285.

44 X. Li, X. Meng, J. Liu, D. Geng, Y. Zhang, M. N. Banis, Y. Li, J. Yang, R. Li, X. Sun, M. Cai and M. W. Verbrugge, *Adv. Funct. Mater.*, 2012, **22**, 1647.

45 C. Wang, D. Wang, Q. Wang and H. Chen, *J. Power Sources*, 2010, **195**, 7432.

46 X. Wang, X. Li, X. Sun, F. Li, Q. Liu, Q. Wang and D. He, *J. Mater. Chem.*, 2011, **21**, 3571.

47 J. Guo, Q. Liu, C. Wang and M. R. Zachariah, *Adv. Funct. Mater.*, 2012, **22**, 803.

48 H. Kim, S. W. Kim, J. Hong, Y. U. Park and K. Kang, *J. Mater. Res.*, 2011, **26**, 2665.

49 L. Wang, Y. Li, Z. Han, L. Chen, B. Qian, X. Jiang, J. Pinto and G. Yang, *J. Mater. Chem. A*, 2013, **1**, 8385.

50 J. F. M. Oudenhoven, L. Baggetto and P. H. L. Notten, *Adv. Energy Mater.*, 2011, **1**, 10.

51 L. Li, C. Nan, J. Lu, Q. Peng and Y. Li, *Chem. Commun.*, 2012, **48**, 6945.

52 M. Kundu, C. C. Ng, D. Y. Petrovykh and L. Liu, *Chem. Commun.*, 2013, **49**, 8459.

53 Q. Hao, J. Wang and C. Xu, *J. Mater. Chem. A*, 2014, **2**, 87.

54 M. A. Lowe, J. Gao and H. D. Abruña, *J. Mater. Chem. A*, 2013, **1**, 2094.

55 D. Yonekura, E. Iwama, N. Ota, M. Muramatsu, M. Saito, Y. Orikasa, W. Naoi and K. Naoi, *Phys. Chem. Chem. Phys.*, 2014, **16**, 6027.

56 S. Grugeon, S. Laruelle, L. Dupont and J. M. Tarascon, *Solid State Sci.*, 2003, **5**, 895.